PASJ: Publ. Astron. Soc. Japan , 1–??,

© 2013. Astronomical Society of Japan.

arXiv:1304.4992v1 [astro-ph.IM] 18 Apr 2013

Toward understanding the anisotropic point spread function of Suprime-Cam and its impact on cosmic shear measurement

Takashi Hamana[1], Satoshi Miyazaki[1], Yuki Okura[1], Tomohiro Okamura[2], Toshifumi Futamase[2]
[1]*National Astronomical Observatory of Japan, Mitaka, Tokyo 181-8588, Japan*
[2]*Astronomical Institute, Tohoku University, Sendai, 980-8578, Japan*

(Received ; accepted)

Abstract

We examine the anisotropic point spread function (PSF) of Suprime-Cam data utilizing the dense star field data. We decompose the PSF ellipticities into three components, the optical aberration, atmospheric turbulence and chip-misalignment in an empirical manner, and evaluate the amplitude of each component. Then, we test a standard method for correcting the PSF ellipticities used in weak lensing analysis against mock simulation. We find that, for long-exposure data, the optical aberration has the largest contribution to the PSF ellipticities, which can be modeled well by a simple analytic function based on the lowest-order aberration theory. Statistical properties of PSF ellipticities originated from the atmospheric turbulence are investigated by using the numerical simulation, and it is found that simulation results are in a reasonable agreement with the observed data. It follows from those findings that the spatial variation of PSF ellipticities consists of two components; one is a smooth and parameterizable component arisen from the optical PSF, and the other is a non-smooth and stochastic component originated from the atmospheric PSF. The former can be well corrected by the standard correction method with polynomial fitting function. However, for the later, its correction suffers from the common limitation arisen from sparse sampling of PSFs due to a limited number of stars. We also examine effects of the residual PSF anisotropies on Suprime-Cam cosmic shear data (5.6-degree^2 of i'-band data). We find that the shape and amplitude of B-mode shear variance are broadly consistent with those of the residual PSF ellipticities measured from the dense star field data. This indicates that most of the sources of residual systematic are understood, which is an important step for cosmic shear statistics to be a practical tool of the precision cosmology.

Key words: cosmology: observations — dark matter — large-scale structure of universe

1. Introduction

Weak gravitational lensing has now became a unique and practical tool to probe dark matter distribution irrespective of its relation to luminous objects, thanks to great progress in technique for weak lensing analysis as well as in wide field imaging instrument (see for reviews Mellier 1999; Bartelmann & Schneider 2001; Refregier 2003; Hoekstra & Jain 2008; Munshi et al. 2008). Measurement of statistics of weak lensing shear, also known as the cosmic shear statistics, has been recognized as one of most powerful probes of the cosmological parameters and is employed as the primary science application by many on-going/future wide field survey projects (e.g., the Panoramic Survey Telescope & Rapid Response System (Pan-STARRS); Dark Energy Survey (DES); Hyper SuprimeCam survey; the KIlo-Degree Survey (KIDS); the Large Synoptic Survey Telescope (LSST); and Euclid mission.) It should be, however, noted that the full potential of the cosmic shear statistics to place a constraint on the cosmological parameters is archived only if systematic errors are reduced down to a required level (Huterer et al. 2006).

In the process of weak lensing analysis, the correction for the point spread function (PSF) is of fundamental importance, because it has two serious effects on galaxy shape measurement: One is the circularization of the images which systematically lower the lensing shear. The other is a coherent deformation of the images caused by anisotropy of the PSF which may mimic a weak lensing shear. A lot of effort has been made to develop techniques and software to correct the PSF effects, and the weak lensing community conducted blind tests using mock data to evaluate their performance (Heymans et al. 2006a; Massey et al. 2007; Bridle et al. 2010; Kitching et al. 2012a,b; and references therein). Most of the softwares are designed to correct the PSF regardless of its origins. Major sources of the PSF, recognized so far except for the diffraction, include the atmospheric turbulence, the optical aberration, the misalignment of CCD chips on a focal plane and the pixelization. Alternative and complementary approach to this issue is to investigate properties of the PSF for a specific instrument with focusing on a specific cause(s), which helps to optimize the PSF correction scheme and to understand a level of residual systematics (Hoekstra 2004; Jarvis & Jain 2004; Wittman 2005; Jarvis, Schechter & Jain 2008; Jee et al. 2007; 2011; Rhodes et al. 2007; Jee & Tyson 2011; Heymans et al 2012; Chang et al. 2003).

The latter approach is exactly what we take in the present paper. The purpose of this study is twofold: First, we investigate properties of anisotropic PSFs of

Subaru prime focus Camera (Suprime-Cam, Miyazaki et al. 2002). We pay a special attention to evaluate the amplitude and spatial correlation of PSF anisotropies caused by different sources. To do this, we use a set of dense star field images from which we can sample the PSF densely and investigate the spatial variation of the PSF in detail. Second, using mock simulation data of PSFs, we examine how well the PSF anisotropy can be corrected with the standard PSF correction scheme.

The motivation of this study is the existence of non-zero B-mode in the cosmic shear correlation functions measured from Suprime-Cam data. The measurement was made by Hamana et al. (2003), they analyzed a 2 degree^2 data and detected statistically significant B-mode correlations (see §5 for an updated but similar result). Since the B-mode shear is not produced by gravitational lensing in the standard gravity theory at the lowest order of the perturbative treatment[1], the existence indicates any non-lensing process(es) taking place. The origin(s) of the B-mode was unclear; it could be simply due to remaining systematics in the data reduction and analysis. Also it may arise from an intrinsic alignment of galaxy shapes (e.g., Croft & Metzler 2000; Catelan, Kamionkowski & Blandford 2001; Crittenden et al. 2002; Jing 2002; Hirata & Seljak 2004; Heymans et al. 2006b). More importantly, the B-mode may be produced by a non-standard gravity. Thus the B-mode shear, in principle, provides us with valuable information on the gravity theory. It is thus important to first understand the level of residual systematic in the data analysis.

The outline of this paper is as follows; in Section 2, data reduction and PSF measurement of dense star field data is described. The amplitude and spatial correlation of PSF anisotropies caused by different sources are evaluated separately in Section 3. The PSF correction scheme adopted in our cosmic shear analysis is tested against the mock simulation data in Section 4. In section 5, we assess the impact of the residual PSF anisotropy on the cosmic shear analysis. Finally, summary and discussion are given in Section 6. In Appendix, we summarize the properties of PSF ellipticities caused by the third-order optical aberrations (Appendix 1), and a numerical study of PSF ellipticities caused by atmospheric turbulence (Appendix 2).

2. Data reduction and PSF measurement of dense star field images

We use i'-band data of a dense stellar field taken with the Suprime-Cam on 2002/9/30, 2003/6/30 and 2003/7/1. The field is located at the Galactic coordinate of $(l, b) = (38^\circ, -3^\circ)$. We collected 289 shots of 60 seconds exposure and 70 shots of 30 seconds exposure from the data archive SMOKA[2]. The seeing FWHMs of those data range from $0.46''$to $0.88''$with the median of $0.63''$.

Each CCD data was reduced using the SDFRED[3] software (Yagi et al. 2002; Ouchi et al. 2004). Note that we conservatively use the data only within 15 arcmin radius from the field center of Suprime-Cam, because at the outside of that, the point spread function (PSF) becomes elongated significantly which may make the correction for the PSF inaccurate. Then mosaicking of 10 CCDs was performed with SCAMP (Bertin 2006) and SWARP[4] (Bertin et al. 2002). In addition to the individual exposure images, we also generate stacked images using SWARP. Note that the images obtained during a same night are taken with the same pointing (thus no dithering was made). Since differences in pointings of images taken in different nights are very small (less than the gaps of CCDs), no data from different CCDs is added.

Object detections were performed with SEXTRACTOR (Bertin & Arnouts 1996) and *hfindpeaks* of IMCAT software (Kaiser, Squires & Broadhurst 1995), and two catalogs were merged by matching positions with a tolerance of 1 arcsec. From the image of stars, we measure an anisotropy of the PSF. We use the following ellipticity estimator (exactly speaking the polarization, see Kaiser et al. 1995) to characterize the anisotropy of PSFs:

$$\boldsymbol{e} = \left(\frac{I_{11} - I_{22}}{I_{11} + I_{22}}, \frac{I_{12}}{I_{11} + I_{22}} \right), \tag{1}$$

$$I_{ij} = \int d^2\theta \; W_G(\theta)\theta_i\theta_j f(\boldsymbol{\theta}), \tag{2}$$

where $f(\boldsymbol{\theta})$ is the surface brightness of an object and $W_G(\theta)$ is the Gaussian window function. We used *getshapes* of IMCAT for the actual computation of these quantities.

From catalogs of detected objects (almost all of them are stars), we generate two kinds of sub-catalogs by mimicking weak lensing analysis: One is "star-role" catalog which contains 700 (the number density of 1 arcmin^{-2}) of the highest SN non-saturated stars. The other is "galaxy-role" catalog which contains 30,000 (42 arcmin^{-2}) of the next highest SN non-saturated stars. The minimum flux SNs for star-role and galaxy-role catalogs are sufficiently high; $\mathrm{SN}_{min} > 330$ and > 40, respectively.

3. Analysis of PSF ellipticities

An anisotropy of PSF is resulted from several sources including the atmospheric turbulence, the optical aberration, the misalignment of CCD chips on a focal plane, the pixelization, and tracking error of the telescope. Our attempt in this section is to examine the PSF on a source-by-source basis using physically motivated models. We evaluate the statistical properties of PSF anisotropies using a two-point correlation function related estimator called the E- and B-mode aperture mass variances defined by (Schneider et al. 1998; we follow the notation by Schneider, van Waerbeke & Mellier 2002)

---

[1] The B-mode shear can arise from higher order terms but their expected amplitude is much smaller than the observed signal (Schneider, van Waerbeke & Mellier 2002; Hilbert et al. 2009).

[2] `http://smoka.nao.ac.jp/`

[3] In the process of the correction for both the field distortion and differential atmospheric dispersion, the bi-cubic resampling scheme was implemented to suppress the aliasing effect (Hamana & Miyazaki 2008).

[4] SWARP was modified so that it can treat the bad pixel flag from the SDFRED software properly.

$$\langle M_{ap}^2\rangle(\theta) = \frac{1}{2}\int_0^{2\theta}\frac{d\phi\phi}{\phi^2}\left[\xi_+(\phi)T_+\left(\frac{\phi}{\theta}\right)+\xi_-(\phi)T_-\left(\frac{\phi}{\theta}\right)\right], \tag{3}$$

and

$$\langle M_{\perp}^2\rangle(\theta) = \frac{1}{2}\int_0^{2\theta}\frac{d\phi\phi}{\phi^2}\left[\xi_+(\phi)T_+\left(\frac{\phi}{\theta}\right)-\xi_-(\phi)T_-\left(\frac{\phi}{\theta}\right)\right], \tag{4}$$

where $T_+(\phi)$ and $T_-(\phi)$ are defined in Schneider et al. (2002), and $\xi_+(\phi)$ and $\xi_-(\phi)$ are the two-point correlation functions of the ellipticities computed by

$$\xi_+(\theta) = \sum_{ij}\left(e_{it}e_{jt}+e_{i\times}e_{j\times}\right)/N_p(\theta) \tag{5}$$

$$\xi_-(\theta) = \sum_{ij}\left(e_{it}e_{jt}-e_{i\times}e_{j\times}\right)/N_p(\theta). \tag{6}$$

In the above expressions, the summation is taken over all the pairs of objects with a distance within a width of a bin considered $\theta-\Delta_{\rm bin}/2<\phi<\theta+\Delta_{\rm bin}/2$, $N_p(\theta)$ is the number of pairs in the bin, and e_t and $e_\times$ are the tangential and 45° rotated ellipticity components in the frame defined by the line connecting a pair of objects.

3.1. *Optical aberrations*

Although the PSF ellipticities arise from several causes and vary temporally, there is a visibly identifiable component that is most likely originated from optical aberrations. In top-left panel of Fig. 1 and 2, we show two examples of *whisker plots* of PSF ellipticities where characteristic features of optical aberration are clearly appeared, and we also show one case in Fig. 3 where optical aberration is almost invisible. We fit the spatial variation of PSFs with the following fitting function of the optical PSF ellipticities which is motivated from the lowest-order optical aberration theory (see Appendix 1 for details),

$$\begin{pmatrix} e_1 \\ e_2 \end{pmatrix} = \begin{pmatrix} c_1 \\ c_2 \end{pmatrix} + \sum_{n_s} s_{n_s} r^{n_s}\begin{pmatrix} \cos 2\psi \\ \sin 2\psi \end{pmatrix} + \sum_{n_a} a_{n_a} r^{n_a}\begin{pmatrix} \cos(\psi-\theta) \\ \sin(\psi-\theta) \end{pmatrix}, \tag{7}$$

where $n_s=\{1,2,3,4\}$ and $n_a=\{1,2\}$. We determine the model parameters s_{n_s}, a_{n_a} and θ by the standard least square method with observed PSF ellipticities. This model consists of the axis-symmetric, asymmetric and constant components, which are displayed in the bottom-left panel, bottom-right panel, and top-right corner of top-panels, respectively. Note that in the top-left panel, the PSF ellipticities measured from "star-role" stars but after a constant component being subtracted are shown. It is clearly seen from Fig. 1 and 2 that the simple three-component model can well reproduce the observed PSFs. It may be therefore said that the optical aberration is one major origin of the PSF anisotropy. Note that a cause(s) of the constant component is uncertain. It arises not only from the optical aberration (the misalignment coma, see

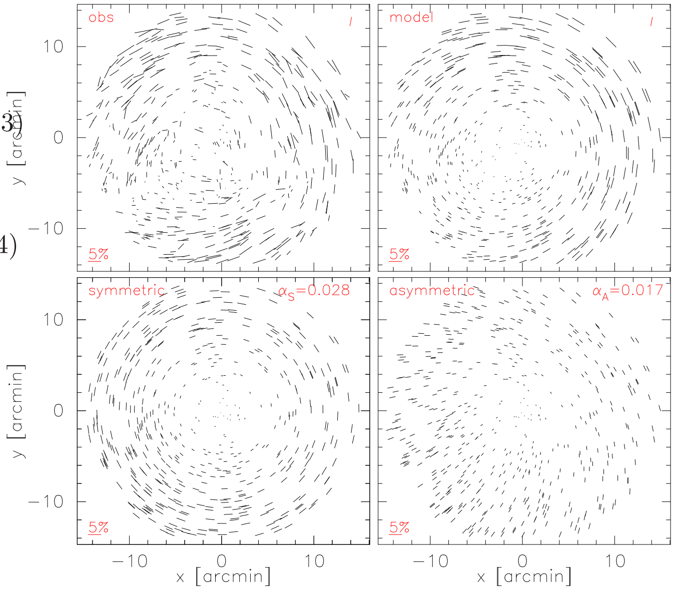

Fig. 1. Ellipticity maps, so-called *whisker plot*, showing an illustrative examples of ellipticity pattern in the Suprime-Cam measured from a 60-second exposure data. The top-left panel shows the observed PSF ellipticites measured from high-SN star images ("star-role" stars), but after the mean component which is displayed in the top-right corner being subtracted. We fit the spatial variation of PSFs with the optical aberration model given by eq. (7). The model consists of the symmetric, asymmetric and constant components. A sum of the first two components is shown in the top-left panel, in which the constant component is plotted in the top-left corner. The bottom-left/right panel shows the symmetric/asymmetric component individually.

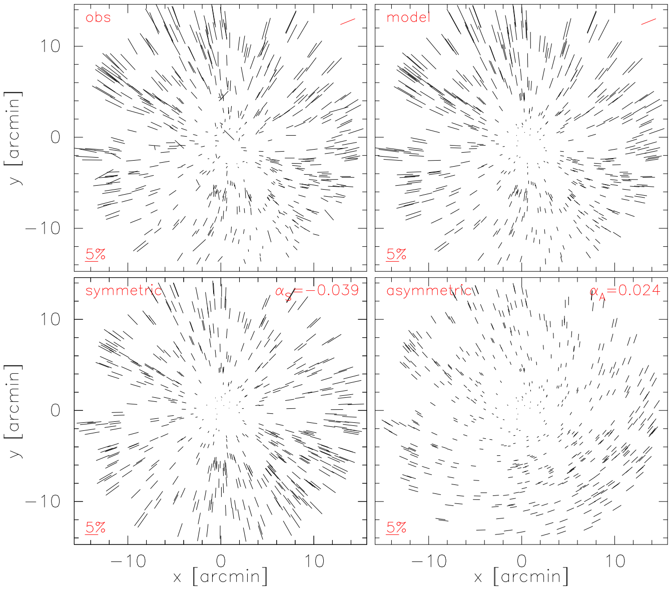

Fig. 2. Same as Fig. 1 but for another 60-second exposure.

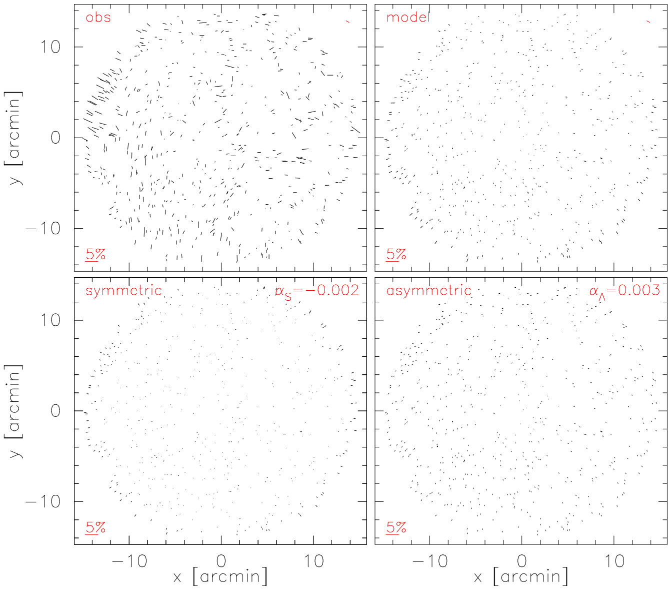

Fig. 3. Same as Fig. 1 but for another 60-second exposure.

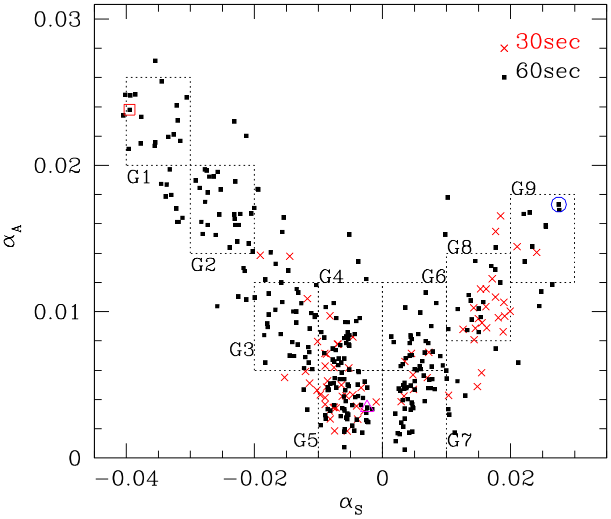

Fig. 4. Scatter plot showing the amplitude of the symmetric and asymmetric components of the optical aberration motivated PSF model for each exposure. Crosses are for 30-second exposures, and small filled squares are for the 60-second exposures. Three examples shown in Fig. 1, 2 and 3 are marked with the open circle, open square and open triangle, respectively. Dotted boxes define groups used for statistical analyses.

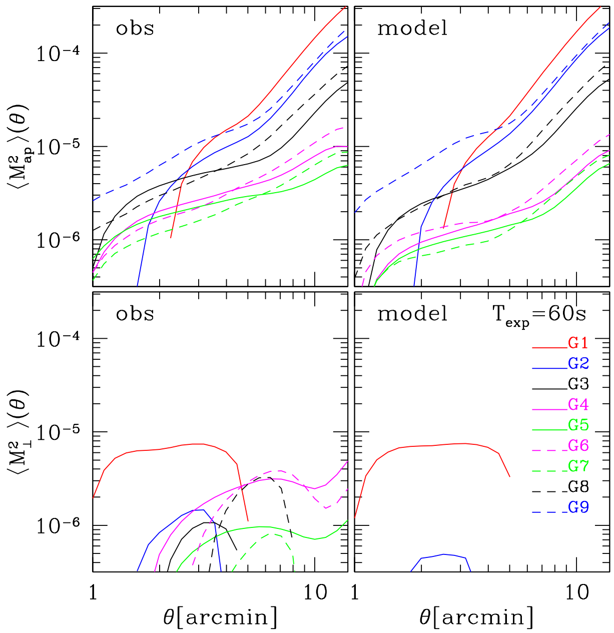

Fig. 5. The aperture mass variance of PSF ellipticities as a function aperture radius. Top and and panels are for E- and B-mode, respectively. The left panels show ones measured from observed data, whereas the right panels are from the optical aberration model. Different lines are for different groups defined in Fig 4, and the plotted aperture mass variances are average values taken over all the exposures in each group.

Appendix 1) but also from, e.g., the tracking error. Since the constant ellipticity component does not contribute to the aperture mass variances, we do not consider it in the following discussion.

Having found that the optical aberration is one major source of the PSF ellipticities and can be well modeled with one constant and two spatially variable components, we introduce estimators that quantify the amplitude of the symmetric and asymmetric components: $\alpha_S = \mathrm{sign}\langle e^2_{sym}\rangle^{1/2}$ and $\alpha_A = \langle e^2_{asym}\rangle^{1/2}$, where the RMS scatter $\langle e^2\rangle^{1/2}$ is computed from the model ellipticities of 700 star-role PSFs for each exposure, and "sign" in α_S is + or − for the tangentially (the mean tangential ellipticity has the plus sign) or radially elongated cases, respectively. The results for all the exposures are plotted in Fig. 4. It is observed from the figure that there is a "V-shaped" trend between strengths of the symmetric component and asymmetric component. In the lowest-order aberration theory, the symmetric aberration is caused by a shift in the focal plane position from an ideal position, whereas the asymmetric one is caused by the decenter and/or tilt between the axes of the focal plane and the corrector (lenses). The result indicates that those two deviations happen in a mutually related manner.

Next we examine the statistical properties of the PSF ellipticities using the aperture mass variance, eqs. (3) and (4) with especially focusing on contribution from the optical aberration. To do so, we classify data using α_S and α_A into 9 groups as shown in Fig. 4. We compute average aperture mass variances for each group and show results in Fig. 5. Left panels of the figure show the results from the observed data, from which it is found that the E-mode variance has a larger amplitude on larger scales, whereas in most cases B-mode variance is smaller than the E-mode especially on larger scales. If we assume a power-law spectrum for ellipticity power spectrum[5] $P_e(l) \propto l^n$,

---

[5] The aperture mass variance relates to the ellipticity power spectrum as (Schneider et al. 1998) $\langle M^2\rangle(\theta) \propto \int dl\ l P_e(l) I^2(l\theta)$ where $I(x)$ is the aperture function. Thus $\langle M^2\rangle(\theta) \propto \theta^{-n-2}$ for a power-law power spectrum of $P_e(l) \propto l^n$.

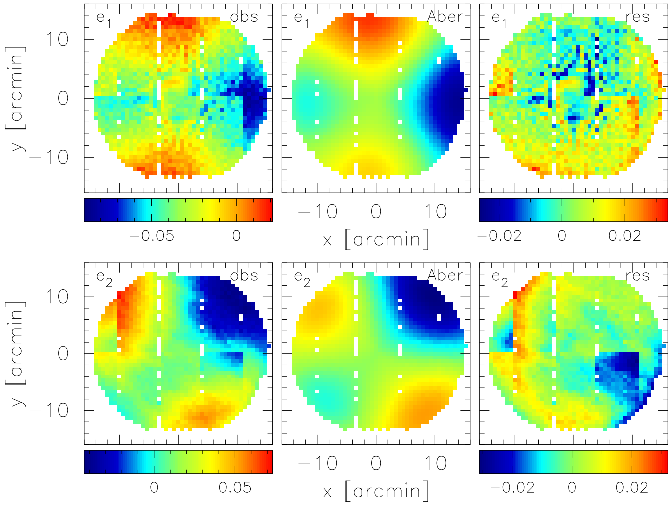

Fig. 6. Ellipticity magnitude for each component is shown: upper and lower panels are for e_1 and e_2, respectively. This is taken form the same data as Fig. 1. The left panels show the observed ellipticity, whereas the central panels show the aberration model. The color scale of the central panels are same as that of the left panels. The right panels show the residual ellipticity ($e_{\rm obs} - e_{\rm opt-model}$). Note that the color scale of the right panels is shown in just bottom of each plot, and are different from the other panels.

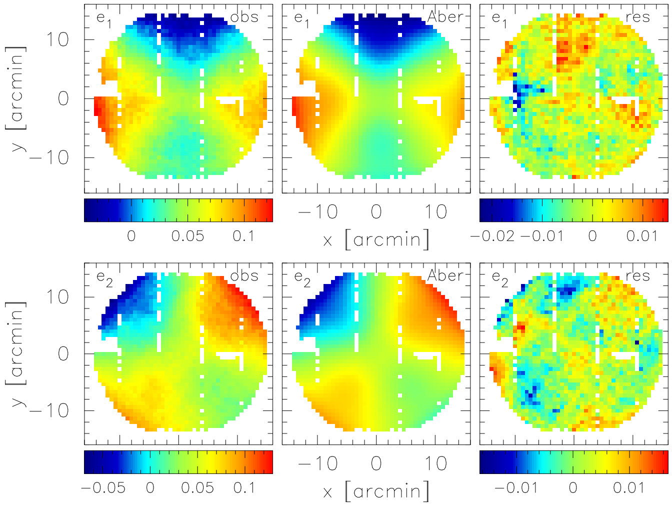

Fig. 7. Same as Fig. 6 but for another data shown in Fig. 2.

the measured E-mode variance indicates that $n \sim -3$.

Right panels of Fig. 5 show the aperture mass variances computed from PSF ellipticities of the optical aberration model. Comparing observed variance in the left panels with ones in the left panels, we can estimate contribution from the optical aberration to PSF ellipticity. We first look at the E-mode. It follows from the comparison between the left and right panel of Fig. 5 that the optical aberration is the dominant component of the PSF ellipticities at least for large aberration cases such like G1-3, G8 and G9 as expected from the visual impression (Figs. 1 and 2). For small aberration cases (G4-G7), one may see the aperture mass variances of the model are slightly smaller than the observed ones. In the following subsections, we argue that the residual variances mostly arise from atmospheric turbulence and chip misalignment. Let's turn to the B-mode. It follows from the comparison between the left and right panel that the variances measured from the model are smaller than the observed ones except for G1. This also suggests an existence of other components than the optical component.

3.2. CCD chip-misalignment

Next, we examine PSF ellipticities remaining after subtracting the optical aberration component. Let us start with visual impression. In Figs. 6 and 7, PSF ellipticities of observed data (left), the optical aberration model (center), and residual of those two ($e_{\rm obs} - e_{\rm opt-model}$) are plotted. Note that the mosaicked data consists of 2-row×5-column CCD chips with masked outer region (beyond 15 arcmin radius from the field center). In those residual plots, there are two apparent features which should be noticed: one is discontinuities between chips, and the other is ripple like patterns. The latter is a characteristic feature of PSF ellipticites caused by atmospheric turbulence and is also observed in CFHT data (Heymans et al. 2012) and in numerical simulation (Jee & Tyson 20011; Chang et al. 2012; 2013; also see Appendix 2), which we will examine in detail in the next subsection 3.3.

In this subsection, we focus on PSF ellipticities caused by misalignment of CCD chips. To do so, we first need to create data that are minimally affected by the optical aberration and atmospheric turbulence. The former could be minimized by using data with small values of both $|\alpha_S|$ and α_A. The latter could be suppressed by stacking many images as the amplitude of the atmospheric PSF decreases with the exposure time as $\langle e^2\rangle^{1/2} \propto T^{-1/2}$ (de Vries et al 2007; Chang et al. 2012; Heymans et al. 2012; see also Appendix 2). Thus we generate a coadded image of 52 shots of 60-sec exposures taken from G5 group where the effect of the optical aberration is in a minimum level and a largest number of shots (52 shots) is contained. The stacking is done using Swarp, and the object detection and ellipticity measurement are done with the same manner as one described in §2.

The PSF ellipticities of the coadded data are shown in Fig. 8. One can see PSF discontinuities between chips even in the observed PSF (top-left panel) as well as in the residual PSFs (top-right panel). We attempt to extract the chip-misalignment component from residual PSF ellipticities by fitting the residual PSFs with the 2nd order bi-polynomial function on the chip-by-chip basis. Derived PSF models are shown in the bottom-right panel of Fig. 8 in which it is seen that characteristic features of chip-misalignment PSF ellipticities (such like discontinuities between chips and chip-scale smooth variation) are well reproduced by the model. We measure the aperture mass variances from the PSF ellipticities and show in Fig. 9. Note that the B-mode variances are too small to analyze

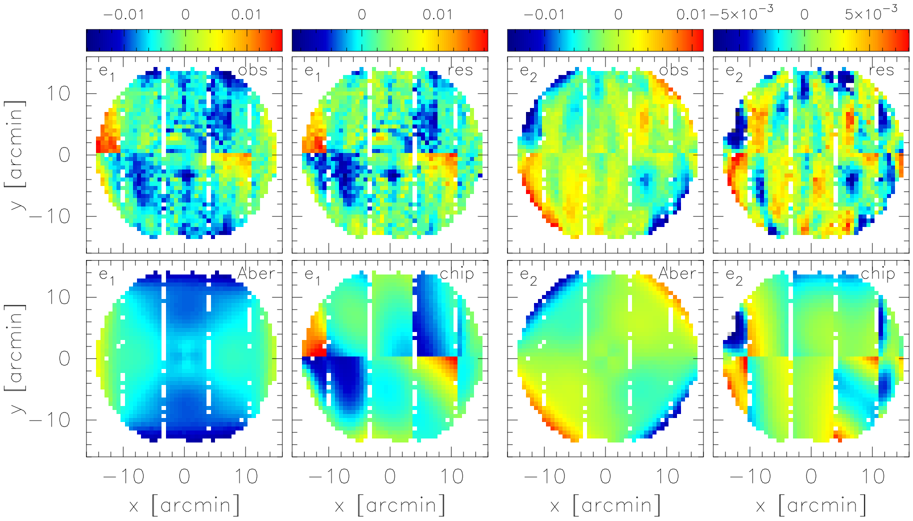

Fig. 8. Ellipticity magnitude for each component is shown: the left and right set of panels are for e_1 and e_2, respectively. Results from a coadded data of 52 60-sec exposures from G5 group are shown. For each set of panels, top-left panel shows an observed ellipticity, bottom-left panel is for the aberration model, top-right panel shows the residual of those two ($e_{\rm obs} - e_{\rm opt-model}$), and bottom-right panel shows the chip-misalignment model described in the section 3.2. Note that the color scale of each column is shown in top of each column.

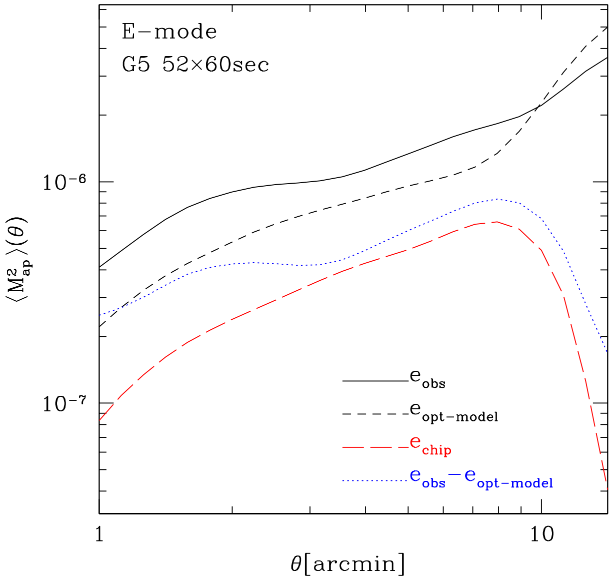

Fig. 9. The E-mode aperture mass variance of PSF ellipticities measured from the coadded data shown in Fig.8. Solid line is for the observed PSFs, dashed line is for the aberration model, the dotted line is for the residual of those two ($e_{\rm obs} - e_{\rm opt-model}$) and long-dashed for chip-misalignment PSF model.

properly and thus we do not present them. Although our model may not extract only the chip-misalignment PSFs but may be affected by other sources of PSF ellipticity, it may be still reasonable to consider that the model allows us to assess an approximate amplitude of the chip-misalignment PSF ellipticies. We read from the Fig. 9 that the amplitude of the chip-misalignment PSF ellipticies is roughly $\langle M_{ap}^2\rangle \sim 10^{-7} \times \theta$. It should be, however, noted that the chip-misalignment PSF is a phenomenon related to the optical aberration and thus its amplitude may vary with deviation in the focal plane position. Therefore the above value should be considered as a characteristic size.

It is also found from Fig. 9 that the aperture mass variance of the residual PSFs ($e_{\rm obs} - e_{\rm opt-model}$) is slightly larger than that of the chip-misalignment PSF model. The amplitude of the excess is roughly $\langle M_{ap}^2\rangle \sim 10^{-7}$. An origin of this excess is not clear, it could be due to imperfection in the models and/or due to atmospheric PSFs and/or due to other causes such like pixelization effects caused in a process of resampling (Hamana & Miyazaki 2008). If the latter is the case, it can be settled by recently developed shape measurements schemes that do not involve a resampling process (e.g., Miller et al. 2007; 2013; and Miyatake et al 2013). Thus we leave it for future work.

3.3. Atmospheric turbulence

Let us turn to the PSF ellipticity originated from atmospheric turbulence. Properties of the atmospheric PSF ellipticity has been examined experimentally (Wittman 2005; Heymans et al. 2012) or using numerical simulations (de Vries et al 2007; Jee & Tyson 20011; Chang et al. 2012; 2013). A major characteristic of the atmospheric PSF ellipticity found from previous studies is that the amplitude of PSF ellipticities decreases with the exposure time as $\langle e^2\rangle^{1/2} \propto T^{-1/2}$ (de Vries et al 2007; Chang et al. 2012; Heymans et al. 2012). Also the shape of the power spectrum and aperture mass variance of the atmospheric PSF ellipticities is investigated numerically (see Appendix 2).

We investigate the atmospheric PSFs using data from the G5 group. In top-panels of Fig. 10, we show the aperture mass variances for different exposure times; from top to bottom, single 30-sec, 60-sec exposures, coadded 4×60, 13×60 and 52×60-sec exposures. As is shown in the plots,

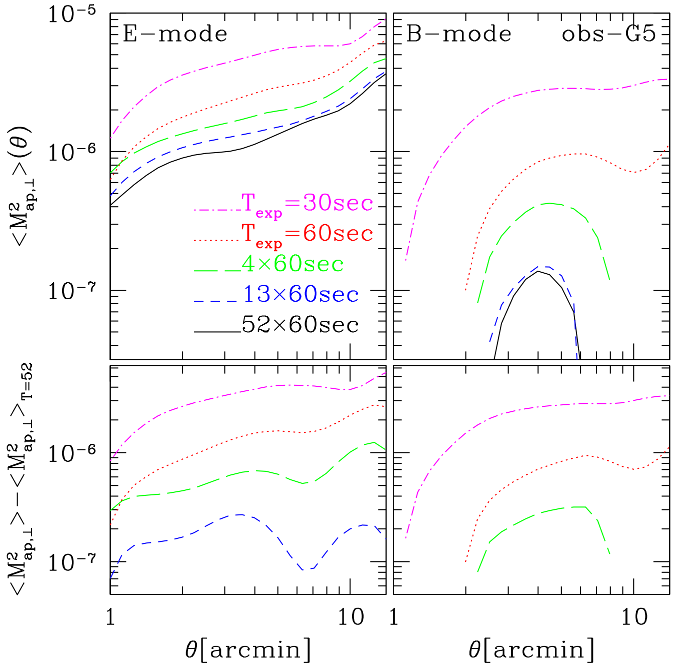

Fig. 10. *Top-panels*: the aperture mass variances of PSF ellipticities measured from data in G5 group for different exposure times; from top to bottom, single 30-sec, 60-sec exposures, coadded 4, 13 and 52 60-sec exposures. *Bottom-panels*: differences between aperture mass variances and one measured from the deepest coadded data.

the amplitude of the aperture mass variance decreases as the exposure time increases. However the minimum amplitude of E-mode is set by the optical aberration PSFs and chip-misalignment PSFs as shown in the last two subsections, whereas the B-mode variance decreases down to $\langle M_\perp^2 \rangle \sim 10^{-7}$. This indicates that the optical and chip-misalignment PSF largely contribute to E-mode PSF ellipticity.

In order to evaluate the amplitude of the atmospheric PSF ellipticities separately from other components, we make a working hypothesis that the amplitude of the deepest data (52×60-sec coadded data) represents an amplitude of (quasi-)static PSF components (such like the optical and chip-misalignment PSFs), and the difference from that gives an estimate of atmospheric PSFs ellipticities. In the bottom-panels of Fig. 10, we plot the differences where one finds that the aperture mass variances have both the exposure time dependence and sharp similar to those obtained from the numerical simulation (Appendix 2). Also, E- and B-mode variances are in the similar amplitude as expected from the numerical simulation. Although the above results are derived relaying on the working hypothesis, those nice agreements would support reasonableness of the hypothesis. We may therefore say that we successfully capture characteristic features of the atmospheric PSF ellipticities in Suprime-Cam data.

4. Testing PSF correction scheme using numerical simulations

Here we investigate how well the PSF ellipticities can be corrected by the standard correction scheme which we describe below. The aim of this study is twofold: One is to understand what sets a lower limit of the anisotropic PSF correction, and the other is to evaluate an amplitude of the residual PSF ellipticities. To do this, we use both the dense star field data and mock data that we describe below.

Before going into details, we briefly describe a basic procedure of the anisotropic PSF correction implemented in actual weak lensing studies so far (see for details, Heymans et al 2006; Massey et al 2007 and references therein): Firstly, PSF ellipticities (or other estimators of PSF) are measured from high-SN star images. In usual weak lensing analyses, a typical number density of stars used for PSF sampling is ~ 1 arcmin^{-2}. Secondly, the spatial variation of PSF ellipticities is modeled by fitting PSF ellipticities with an analytic function such like the polynomial. Then finally, an artificial shape deformation in galaxy images caused by the PSF is corrected using the PSF model delivered by the analytic function. Although an actual implementation of the above procedure depends on technique of weak lensing analysis (Heymans et al 2006; Massey et al 2007), there is one common limitation which comes from a sparse sampling of stars, namely, the spatial variation of PSFs on scale smaller than the mean star separation is poorly sampled, and as a result, small scale components in the PSF anisotropy are hardly corrected.

Our PSF correction scheme is based on the KSB algorithm (Kaiser et al 1995; Hamana et al. 2003; Heymans et al 2006) and we refer the reader to the above references for details. Here we only describe some details in implementation which are specific to this study. We use bi-variable polynomial function for modeling the spatial variation of PSF ellipticites. We divide data into 2×2 regions or into each CCD chip, and a PSF model is generated for each sub-region. The order of polynomial is set 4th for 2×2-division and 2nd or 3rd for the chip-basis case. The 2×2-division is taken because in our actual cosmic shear analysis the PSF correction is made on a sub-region basis with a similar area, whereas the chip-basis analysis is taken to test its ability of improving the anisotropic PSF correction.

Let us start with a simpler situation using mock PSF ellipticity catalogs. The mock data have the same geometry and number of objects as those of the dense star field data, that is 700 "star-role" objects and 30,000 "galaxy-role" objects (see §2). Instead of generating mock image, we simply generate object catalogs. Each object has items; the positions, and 3-component PSF ellipticities including optical, atmospheric, and CCD-misalignment components denoted by $e_{\rm opt}$, $e_{\rm atm}$ and $e_{\rm chip}$, respectively. The optical component is made by using the optical aberration motivated model, eq. (7), introduced in Appendix 1, and we adopted model parameters for G5 group in §3.1. For the CCD-misalignment component, we adopt the 2nd-order

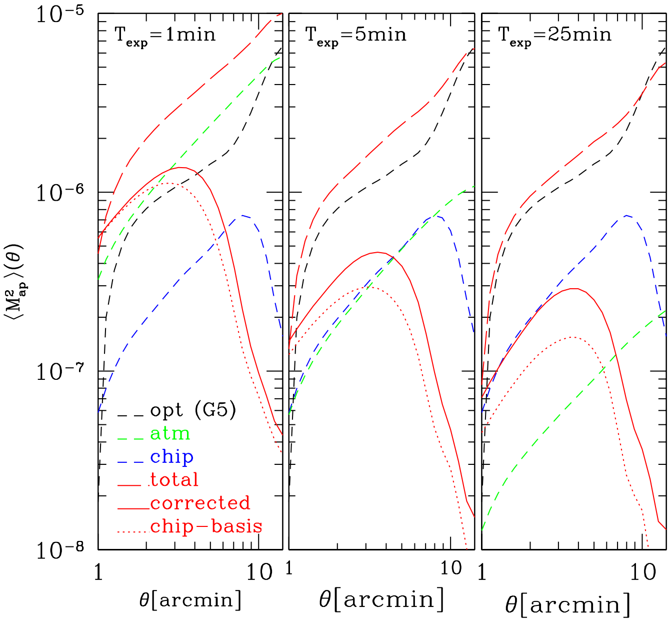

Fig. 11. E-mode aperture mass variances of PSF ellipticities before and after anisotropic PSF correction obtained from the mock simulations. Dashed lines are for three input PSF models including the optical (black), atmospheric (green) and the CCD-misalignment components. The long-dashed lines is for total of these three components. The solid line shows one after the correction based on the 2×2-division, whereas the dotted line is for the chip-basis. From left to right, the exposure time is 1, 5 and 25 minutes, respectively.

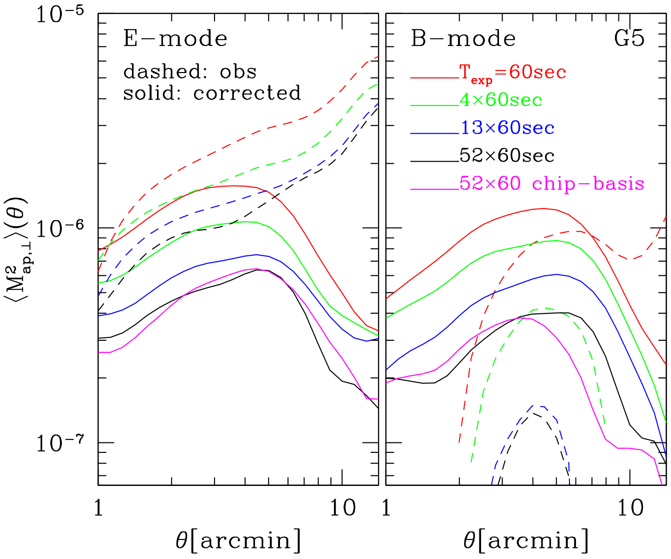

Fig. 12. E- (left) and B-mode (right) aperture mass variances of PSF ellipticities before (dashed curves) and after (solid curves) the anisotropic PSF correction. The results obtained from the G5 group are presented for various exposure time. The PSF correction is made on a basis of 2×2 sub-regions except for the magenta curve which is for the chip-basis correction.

polynomial models obtained in §3.2. The atmospheric component is modeled by the random field with the power-law power spectrum of the power-law index of -3 based on our finding (see §2 and Appendix 2). Its amplitude is set by the empirical relation of eq. (A4) for the exposure times of 1, 5, and 25 minutes. We compute the total ellipticity by simply adding the three components, instead of treating in the convolution manner. This is a reasonable approximation because each ellipticity component is small. Then, the anisotropic PSF correction is made for mock catalogs in the procedure described above.

The results from the mock simulation are presented in Fig. 11, from which the following three points are seen. First, as mentioned above, the mean separation of stars (~ 1 arcmin), which are used to model the spatial variation of PSFs, sets a fundamental limitation on the PSF correction. In the case of the aperture mass, its window function is most sensitive to fluctuations on scales $\sim 1/5$ of the aperture size (Schneider et al. 1998), This defines a characteristic aperture scale of $\theta \sim 5$ arcmin, and on scales larger than that the correction works very well but on smaller scale it does very poorly. This is especially the case for the atmospheric PSF. Second, in spite of the above limitation, the optical components is well corrected even on smaller scales. The reason of this is the smoothness of the optical component; as has been found in §3.1, the spatial variation of the optical PSFs can be well fitted by a polynomial-based model. Thus even with a sparse sampling, it can be well modeled with the polynomial function. Third, for 2×2-division case, the CCD-misalignment component combined with the optical component sets a limit on the anisotropic PSF correction. This is a natural consequence that even each individual component is smooth and is modeled by polynomial function, the mixed PSFs may be no longer simple and thus may not be corrected by the polynomial model. This can be partly avoided by adopting the chip-basis correction as is seen in the right panel of the Fig 11, though the residual variance does not reach to the level of the atmospheric PSF. A further improvement of the PSF correction may be achieved by recently proposed correction schemes (e.g., Chang et al. 2012; Bergé et al. 2012; Gentile, Courbin & Meylan 2013), and we leave it for future study. The above three findings provide us with a clue to interpret a result obtained from an analysis of real data.

Let us turn to the analysis of the dense star field data. In Fig. 12, the aperture mass variances measured from the G5 group data (defined in Fig. 4) are presented for different exposure times, where the anisotropic PSF correction is made on a basis of 2×2 sub-regions except for the magenta curve to which the chip-basis correction is applied. From the figure, the following four findings are obtained: Firstly, it is found that after the PSF correction E- and B-mode are almost equally partitioned, regardless of properties of raw PSF ellipticities. A plausible reason of this is that E- and B-mode are mixed up in the process of the PSF correction. Secondly, the result of 60-sec exposure is in a good agreement with that of the mock simulation. But at a closer look at larger scales, it is found that the residual aperture mass variance falls less quickly than the mock result, indicating that the spatial variation of real PSF ellipticities is more complex than one assumed in the mock simulation. Thirdly, as expected from the result of the mock simulation,the residual aperture mass variance decreases with increasing the exposure time. However, the decrement is less than what expected from the mock simulation. Finally, it is found from the comparison of two different correction schemes for 52-coadded data that the chip-basis correction little makes an improvement over the other case. It is speculated from the last two points combined with the findings from the mock simulation (that is, an existence of a non-smooth component sets a lower limit of the correction on scales smaller than mean separation of stars) that there exists unidentified PSF ellipticity component(s) whose amplitude is greater than the chip component found in §3.2 (see also Fig. 9). Although an origin of the unknown PSF component is not clear, the above result provides us with an empirical estimate of *the "best performance"* of the PSF correction scheme that we adopted in this paper.

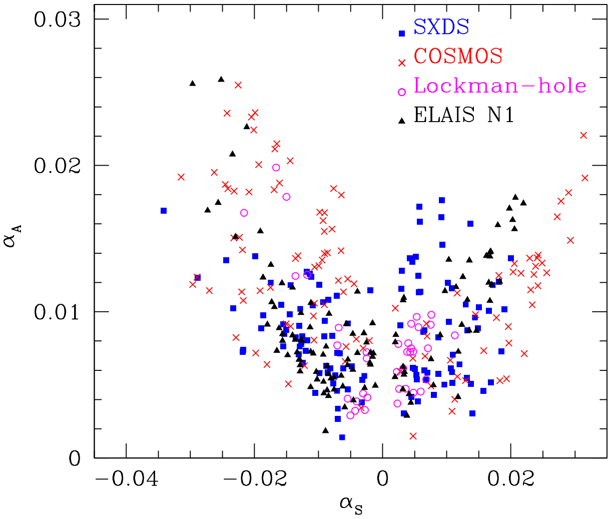

Fig. 13. Same as Fig. 4 but for data used for the cosmic shear analysis. The optical model fitting is applied to individual exposures. The exposure time of each exposure is $120-420$ seconds. Different symbols are for different fields.

5. Residual PSF anisotropies in Suprime-Cam cosmic shear data

Here we examine effects of the residual PSF anisotropies on Suprime-Cam cosmic shear data. To do so, we measure the E- and B-mode shear aperture mass variance from 5.6-degree^2 Suprime-Cam deep imaging data, and compare the B-mode shear variance with the residual PSF ellipticities measured from the dense star field in §3.

5.1. *Suprime-Cam data and weak lensing analysis*

We use the same data as those used in Hamana et al (2012) in which basics of data and data analyses are described. Therefore here we only describe points specific to this work. Suprime-Cam i'-band data are corrected from the data archive, SMOKA, under the following three conditions: data are contiguous with at least four pointings, the total exposure time for each pointing is longer than 1800 sec, and the seeing full width at half-maximum (FWHM) is better than 0.65 arcsec. Four data sets (named by SXDS, COSMOS, Lockman-hole and ELAIS-N1) meet these requirements. The exposure times of individual exposures range from 120 and 420 seconds. Data reduction, mosaic stacking and object detection were done with the same procedure described in §2. The effective area after masking regions affected by bright stars is 5.57 degree^2. Depth of the coadded images varies among four fields, and it is found that the number counts of faint galaxies are saturated at AB magnitude of $i' = 25.2 - 25.5$.

For weak lensing measurements, we adopt the so-called KSB method described in Kaiser et al. (2005), Luppino & Kaiser, and Hoekstra et al (1998) with some modifications being made following recent developments (Heymans et al. 2006a; Massey et al. 2007). Stars are selected in a standard way by identifying the appropriate branch in the magnitude half-light radius (r_h) plane, along with the detection significance cut $S/N > 10$. The number density of stars is found to be ~ 1 arcmin^{-2} for the four fields. We only use galaxies met the following three conditions, (i) the detection significance of $S/N > 3$ and $nu > 10$ where nu is an estimate of the peak significance given by *hfindpeaks*, (ii) r_h is larger than the stellar branch, and (iii) the AB magnitude is in the range of $22 < i' < 25$. The number density of resulting galaxy catalog is ~ 23.5 arcmin^{-2} and is quite uniform among four fields. We measure the shape parameters of objects by *getshapes* of IMCAT. The PSF correction is done on a sub-field basis, where the coadded data were divided into sub-fields of about 15×15 arcmin^2 (approximately one fourth of the Suprime-Cam's field-of-view). The spatial variation of PSF ellipticites measured from stars are modeled with the 4th order bi-polynomial function, and the PSF model combined with the smear polarizability tensor (P_{sm}) of each galaxy is used to correct the PSF ellipticities of galaxies. In KSB formalism, the shear (we denote by γ) is related to the observed ellipticity through the shear polarizability tensor, P_γ, which is evaluated by the smoothing and weighting method developed by Van Waerbeke et al. (2000; see Hamana et al 2003 for an actual implementation of this method).

Before presenting the shear aperture mass variance measured from coadded data, it is worth looking into PSF ellipticities of individual exposures. To do so, we generate mosaicked data of individual exposures and select stars in the same procedures as described above. The spatial variation of PSF ellipticities measured from the stars are fitted to the optical model, eq. (7), and the amplitude of the symmetric and asymmetric components of the model are evaluated (see §3.1 and Appendix 1 for details). The results are plotted in Fig. 13, in which one may see "V-shaped" trend similar to the results obtained from the dense star field data (Fig. 4), though the scatter is somewhat larger for this case. This similarity implies that knowledge of the PSF anisotropy learned from the dense star field analysis (§3) is applicable to cosmic

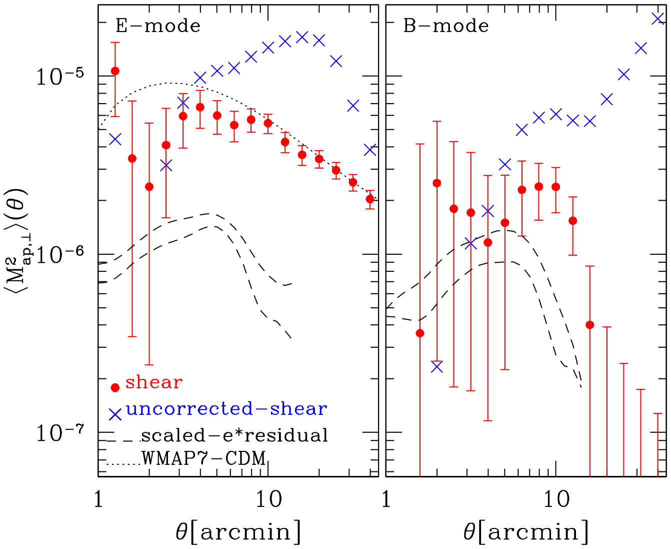

Fig. 14. Filled circles show E- (left) and B-mode (right) shear aperture mass variances measured from faint galaxies. The error bars present the statistical error computed from 100 randomized realizations. The crosses are for *uncorrected-shears* (the galaxy shears to which the correction for the PSF anisotropy is not applied). The dashed curves shows variances of the residual PSF ellipticities (but scaled to the shear by multiplying a factor $(\langle P_{sm}/P_\gamma\rangle/\langle P^*_{sm}\rangle)^2 \simeq 1.5^2$) measured from the G5 group of the dense star field data (see §3 and Fig. 12); the upper and lower curves are for 13×63 and 52×60-sec exposure, respectively. The dotted curve shows the ΛCDM prediction based on the 7-year WMAP cosmological model with the source galaxy redshift distribution inferred from COSMOS photometric redshift catalog.

shear analyses. It should be however noticed that there is one component that is not taken into consideration in the dense star field analysis, namely stacking of multiple dithered exposures. It is obvious that stacking of dithered exposures makes the spatial variation of PSFs complicated which may result in a poorer anisotropic PSF correction. We will return to this point later.

5.2. *Cosmic shear aperture mass variance*

We compute the E- and B-mode aperture mass variance of galaxy shears through the two-point correlation functions using eqs. (3)-(5) with the summations in eq. (5) being replaced with the weighted summation, $\sum w_i w_j \gamma_i \gamma_j / \sum w_i w_j$ where w_i is the weight for i-th galaxy. In addition to the shear, we compute the *uncorrected-shear*, that is, the galaxy shear to which the correction for the PSF anisotropy is not applied. The results are presented in Fig. 14. The error bars indicate the root-mean-square among 100 randomized realizations, in which the orientations of galaxies are randomized, and presumably represent the statistical error coming from the galaxy shape noise. It is found from Fig. 14 that the B-mode shear variance is non-zero on the aperture scale of $\theta \lesssim 10$ arcmin. It should be noted that adjacent bins are correlated. In order to compare the shear variances with those of the residual PSF ellipticites, we transform the star ellipticity to the galaxy shear by multiplying a factor $\langle P_{sm}/P_\gamma\rangle/\langle P^*_{sm}\rangle$ which is found to be $\simeq 1.5$ (thus $\gamma^* \simeq 1.5e^*$). The results from the G5 group of the dense star field data with the 2×2 sub-region basis correction (see §3 and Fig. 12) are also shown in Fig. 14. The upper and lower curves are for 13×60 seconds and 52×60 seconds exposure, respectively. Since the total exposure times of four cosmic shear fields are $2400-6000$ seconds, the lower curve could be considered as a "*best performance*" of our PSF ellipticity correction scheme. The B-mode shear signals at smaller scales ($\theta \lesssim 10$ arcmin) are larger than this expectation. A possible reason of this excess is that stacking of dithered multiple exposures which is not involved in the dense star field analysis. This issue will be investigated in detail in a future study in which we will adopt a PSF correction scheme on an individual exposure basis. On the other hand, the B-mode variance drops at larger scales ($\theta \gtrsim 15$ arcmin), which is in nice agreement with one expected from the dense star field analysis. It is however noticed that in the case of the dense star field data, the turnaround aperture scale is about 5 arcmin which is naturally set by the mean separation of stars (∼ 1 arcmin) (see §4), whereas it is about 10 arcmin for the cosmic shear data. The reason of this is unclear, it could be related to an excess B-mode uncorrected shear variance observed at ∼ 10 arcmin.

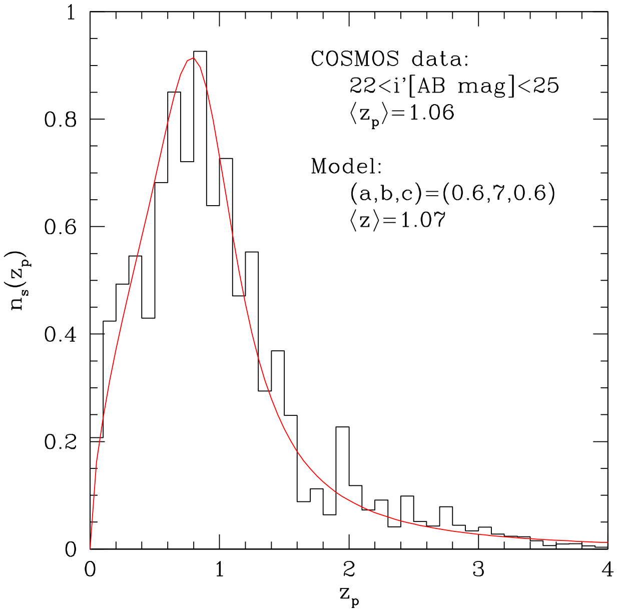

Fig. 15. Redshift distribution of galaxies used for the cosmic shear analysis derived adopting the COSMOS photometric redshift catalog (Ilbert et al 2009). The solid curve shows the fitting model by eq. 8 with the parameters denoted in the panel.

Since the anisotropic PSF correction works well on larger scales, it is interesting to compare the E-mode variance with the theoretical prediction on those scales. we derive the redshift distribution of source galaxies, which is an essential ingredient for computing a theoretical model, in the following manner: We utilize the COSMOS field data. We merge the galaxy catalog used for the cosmic shear measurement with the COSMOS photometric redshift catalog (Ilbert et al 2009), and compute the redshift distribution adopting the photometric redshift, which is presented in Fig. 15. We fit the redshift distribution with the following function (Fu et al. 2008)

$$n(z) = A\frac{z^a + z^{ab}}{z^b + c}, \tag{8}$$

where the normalization A is determined by imposing $\int dz\ n(z) = 1$ within the integration range $0 < z < 6$. We find that a parameter set $(a,b,c) = (0.7, 6.0.7)$ gives a reasonably good fit to the data as shown in Fig. 15. The mean redshift of this model is 1.07 which is in a very good agreement with the value derived from the photometric redshift data ($\langle z_p \rangle = 1.06$). We plot in Fig. 14 the ΛCDM prediction based on the 7-year WMAP cosmological model (Komatsu et al. 2011). For the nonlinear CDM power spectrum, we use the HALOFIT model by Smith et al. (2003). It is seen in Fig. 14 that the measured E-mode shear variance is in a nice agreement with the theoretical model on the scales where the anisotropic PSF correction works well ($\theta > 15$ arcmin). One may be interested in a constraint on the cosmological parameters to be placed from the data. However, to derive that, there are some issues to be carefully taken into consideration; for example, an effect of the noise bias (Refregier et al. 2012; Melchior & Viola 2002; Okura & Futamase 2012) and the covariance matrix of cosmic shear correlation function including non-Gaussian contributions (Sato et al., 2009; 2011). Those are beyond of the scope of this paper, and will be examined in a future work.

6. Summary and discussion

We have analyzed the anisotropic PSF of Suprime-Cam data utilizing the dense star field data. We have decomposed the PSF ellipticities into three components, the optical aberration, atmospheric turbulence and chip-misalignment in an empirical manner, and have assessed the amplitude of each component. Then, we have tested a standard method for correcting the PSF ellipticities against mock simulation which is based on models of the PSF ellipticities obtained from the dense star field data analysis. Finally we have examined the impact of the residual PSF ellipticities on cosmic shear measurement.

We have found that the optical aberration has the largest contribution to the PSF ellipticities of long-exposure (say, longer than 10 minutes) data. We have also found that the spatial variation of the optical PSFs can be modeled by the simple three-component model which is based on the lowest-order aberration theory described in Appendix 1. It is also found that the optical PSF ellipticities vary smoothly on the focal plane, and thus are well corrected by the standard correction method in which the spatial variation is modeled by a polynomial function.

The PSF ellipticities after subtracting the optical PSF model ellipticities show discontinuities between CCD chips, which indicates that the misalignment of chips on the focal plane induces an additional PSF ellipticity. In order to make a crude estimation of the amplitude of chip-misalignment PSF ellipticities, we have fitted the residual PSF ellipticities to the 2nd order bi-polynomial function on chip-by-chip basis. It turns out that the amplitude of the chip-misalignment PSF ellipticities is lower than the optical component, though it is not negligible. It is found from the mock simulation that the chip-misalignment component combined with the optical component puts a lower limit on the capability of the PSF correction, which can be, in principle, avoided by employing a chip-basis correction scheme.

We have investigated properties of PSF ellipticities originated from the atmospheric turbulence using the numerical simulation of wave propagation through atmospheric turbulence under a typical weather condition of Subaru telescope at Mauna-kea (Appendix 2). From the simulation results, we have evaluated the power spectrum and aperture mass variance of atmospheric PSF ellipticities, and have derived power-law fitting functions of them. As was already pointed out in literatures (Wittman 2005; de Vries et al 2007; Jee & Tyson 20011; Chang et al. 2012; 2013 Heymans et al. 2012), the RMS amplitude of the atmospheric PSF ellipticities decreases as $T_{exp}^{-1/2}$. We computed the aperture mass variance of the dense star field data for various exposure time (from 30-sec to 52×60-sec). The amplitude of the atmospheric PSF ellipticities was evaluated by assuming the deepest data represents an amplitude of (quasi-)static PSF components, and the difference from that is due to the atmospheric PSFs ellipticities. The results are found to be in a reasonable agreement with the simulation results. Therefore, we may conclude that the aperture mass variance of the atmospheric PSF ellipticies for a long-exposure data (say, longer than 10 minutes), is at least one order of magnitude smaller than that of the optical PSF ellipticities. Since the atmospheric PSFs are not smoothly varying component, its correction suffers from the common limitation that the PSF correction on scales smaller than the mean star separation works very poorly because of the spatial variation of PSFs on those scales is hardly sampled.

The above findings provide us a clue to develop an optimal PSF interpolation scheme: It is found that the spatial variation of PSF ellipticities consists of two components; one is a smooth and parameterizable component arisen from the optical aberration and chip-misalignment, and the other is a non-smooth and stochastic component arisen from the atmospheric PSFs. The former can be modeled with a parametric model as shown in this paper. Also it has been argued that an interpolation scheme based on the principle component analysis is effective for such a case (Jarvis & Jain 2004; Jee & Tyson 2011; see also Miyatake et al 2013 and Lupton et al 2001 for an actual implementation for Suprime-Cam data reduction pipeline). On the other hand, it has been shown in Bergé, et al (2012) and Gentile et al. (2013) that a local type correction scheme such as the radial basis functions and Kriging works well for the atmospheric PSFs. Apparently, a hybrid interpolation scheme, in which the above two types of interpolation schemes are optimally incorporated, is a strong candidate for achieving a better PSF correction.

We have examined effects of the residual PSF anisotropies on Suprime-Cam cosmic shear data. We have compared the B-mode shear variance measured from 5.6-degree^2 i'-band data with the residual PSF ellipticities (but being properly transformed into shear) measured from the dense star field data, which can be considered as the "best performance" of our PSF ellipticity correction scheme. It is found that the shape and amplitude of B-mode shear variance are broadly consistent with those of the residual PSF ellipticities. This indicates that most of the sources of residual systematic are understood, which is an important step for cosmic shear statistics to be a practical tool of the precision cosmology. However it is also found that the B-mode shear amplitude at scales ~ 10 arcmin are systematically larger than the residual PSF. A reason of this excess is unclear, one possible reason is that stacking of dithered multiple exposures which is not involved in the dense star field analysis. Such stacking related issues may be avoided by employing a weak lensing shape measurement scheme on the basis of individual exposures (e.g., Miller et al. 2007; 2013; and Miyatake et al 2013), which combined with a hybrid interpolation scheme will be addressed in a future work.

We greatly thank Y. Miller for many fruitful discussions on various aspects of this work. We thank M. Takada, M. Oguri and H. Miyatake for useful discussions. We thank Y. Utsumi for help with photometric calibration of Suprime-Cam data. We also thank L. Van Waerbeke and R. Mandelbaum for valuable comments on on an earlier manuscript which improved the paper. We would like to thank M. Britton for making the ARROYO software available. Numerical computations in this paper were in part carried out on the general-purpose PC farm at Center for Computational Astrophysics, CfCA, of National Astronomical Observatory of Japan. This work is based in part on data collected at Subaru Telescope and obtained from the SMOKA, which is operated by the Astronomy Data Center, National Astronomical Observatory of Japan. This work is supported in part by Grant-in-Aid for Scientific Research from the JSPS Promotion of Science (23540324).

References

Bartelmann M., Schneider P., 2001, Physics Report, 340, 291
Bergé J., Price S., Amara A., Rhodes J., 2012, MNRAS, 419, 2356
Bertin E., Arnouts S., 1996: A&AS, 317, 393
Bertin E., Mellier Y., Radovich M., Missonnier G., Didelon P., Morin B., 2002, ASP Conference Proceedings, 281, 228
Bertin E., 2006, ASP Conference Series, 351, 122
Bridle S. et al. 2010, MNRAS, 405, 2044
Britton, M. C., 2004, Proc. SPIE, 5497, 290
Catelan P., Kamionkowski M., Blandford R. 2001, MNRAS, 320, 7
Chang et al, 2012, MNRAS, 427, 2572
Chang et al, 2013, MNRAS, 428, 2695
Crittenden R., Natarajan P., Pen U., Theuns T. 2002, ApJ, 559, 552
Croft R., Metzler C. 2000, ApJ, 545, 561
de Vries W. H., Olivier S. S., Asztalos S. J., Rosenberg L. J., Baker K. L., 2007, ApJ, 662, 744
Ellerbroek B. L., Rigaut F. J., 2000, Proc. SPIE, 4007, 1088
Fu et al., 2008, A&A, 479, 9
Gentile M. Courbin F., Meylan G., 2013, A&A, 549, A1
Hamana T., et al, 2003, ApJ, 597, 98
Hamana T., Miyazaki S., 2008, PASJ, 60, 1363
Hamana T., Oguri M., Shirasaki M., Sato M., 2012 MNRAS 425, 2287
Hardy J. W., 1998, "Adoptive Optics for Astronomical Telescopes" Oxford University Press
Heymans C., et al. 2006, MNRAS, 368, 1323
Heymans C., White M., Heavens A., Vale C., van Waerbeke L., 2006, MNRAS, 371, 750
Heymans C., Rowe B., Hoekstra H., Miller L., Erben T., Kitching T., van Waerbeke L., MNRAS, 421, 381
Hilbert S., Hartlap J., White S. D. M., Schneider P., A&A, 499, 31
Hirata C., Seljak U., 2004, Phys. Rev. D, 70, 063526
Hoekstra H., 2004, MNRAS, 347, 1337
Hoekstra H., Franx M., Kuijken K., Squires G., 1998, ApJ, 504, 636
Hoekstra H., Jain B., 2008, Annual Review of Nuclear and Particle Systems, 58, 99
Huterer D., Takada M., Bernstein G., Jain, B., 2006, MNRAS, 366, 101
Ilbert O., et al., 2009, ApJ, 690, 1236
Jarvis M., Jain B., 2004, submitted to ApJ (arXiv:astro-ph/0412234)
Jarvis M., Schechter P., Jain B., 2008, submitted to PASP (arXiv:0810.0027)
Jee M. J., Tyson J. A., 2011, PASP, 123, 596
Jee, M J., Blakeslee J. P., Sirianni M., Martel A. R., White R. L., Ford H. C., 2007, PASP, 119, 1403
Jing Y., 2002, MNRAS, 335, 89
Kaiser N., Squires G., Broadhurst T., 1995, ApJ, 449, 460
Kaiser N., Torny J. L., Luppino, G., A., 2000, PASP, 122, 768
Kitching T. D., et al, 2012a, MNRAS, 423, 3163
Kitching T. D., et al, 2012b, ApJS submitted (arXiv/2012.1979)
Komatsu E., et al., 2011, ApJS, 192, 18
Luppino G. A., Kaiser N., 1997, ApJ, 475, 20
Lupton R., Gunn J. E., Ivezic Z., Knapp G. R., Kent S., Yasuda N., 2001, in Harnden F. R. Jr, Primini F. A., Payne H. E., eds, ASP Conf. Ser. Vol. 238, Astronomical Data Analysis Software and Systems X. Astron. Soc. Pac., San Francisco, p. 269
Massey, R., et al., 2007, MNRAS, 376, 13
Mellier Y., 1999, Annu. Rev. Astron. Astrophys., 37, 127
Melchior P., Viola M., 2012, MNRAS, 424, 2757
Miller L., Kitching T. D., Heymans C., Heavens A. F., van Waerbeke L., 2007, MNRAS, 382, 315
Miller L., et al, 2013, MNRAS, 429, 2858
Miyatake, H., et al, 2013, MNRAS, 429, 3627
Miyazaki S. et al., 2002, PASJ, 54, 833
Munshi D., Valageas P., van Waerbeke L., Heavens A., 2008, Physics Report, 462, 67
Okura Y., Futamase T., 2012, subitted to ApJ (arXiv:1208.3564)
Ouchi, M., et al. 2004, ApJ, 611, 660

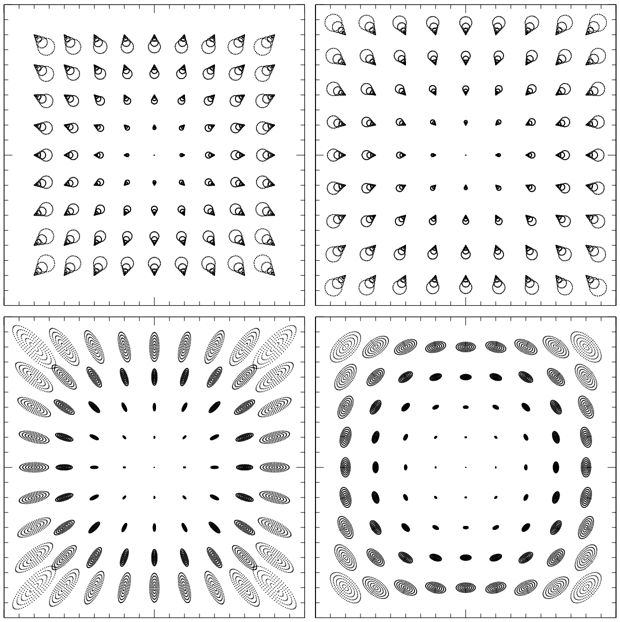

Fig. 16. *Top two panels*: spot diagrams for the Seidel coma with opposite signs of W_{131}. In both cases, the major axis of the ellipticity of the PSF are radially oriented with a scaling of $|e| \propto r^2$. *Bottom two panels*: spot diagrams for a combination of astigmatism and field curvature: Bottom-left panel is for a case for $|W_{222}+W_{220}| > |W_{220}|$ where are the bottom-right panel is for $|W_{222}+W_{220}| < |W_{220}|$. In both cases, the ellipticity parameter is scaled as $|e| \propto r^4$.

Saha S. K., 2007, "Diffraction-Limited Imaging with Large and Moderate Telescope" World Scientific

Sato M., Hamana T., Takahashi, R., Takada M., Yoshida N., Matsubara T., Sugiyama N., 2009, ApJ, 701, 945

Sato M., Takada M., Hamana T., Matsubara T., 2011, ApJ, 734, 76

Schneider P., van Waerbeke L. Jain B., Kruse G., 1998, MNRAS, 296, 873

Schneider P., van Waerbeke L., Mellier Y., 2002, A&A, 389, 729

Smith R. E., Peacock J. A., Jenkins A., White S. D. M., Frenk C. S., Pearce F. R., Thomas P. A., Efstathiou G., Couchmann H. M. A., 2003, MNRAS, 341, 1311

Thompson K., J. 2005, Opt. Soc. Am. A., 22, 1389

Refregier A., 2003, Annu. Rev. Astron. Astrophys., 41, 645

Refregier A., Kacprzak T., Amara A,m Bridle S., Rowe B., 2012, MNRAS, 425, 1951

Rhodes J., et al. 2007, ApJS, 172, 203

Wittman, D. 2005, ApJ, 632, L5

Yagi, M., et al. 2002, AJ, 123, 66

Appendix 1. PSF ellipticity originated from the third-order optical aberrations

We summarize the properties of ellipticity in the PSF caused by the third-order optical aberrations with and without rotational symmetry. We consider a system with a circular pupil. We follow the notation by Thompson (2005; see Fig 1 of his paper): $\vec{H}$ represents the position in the image field and without loss of generality we can choose $(H_x, H_y) = (0, h)$. $\vec{\rho}$ represents the position in the exit pupil with $(\rho_x, \rho_y) = (\rho \sin\phi, \rho \cos\phi)$.

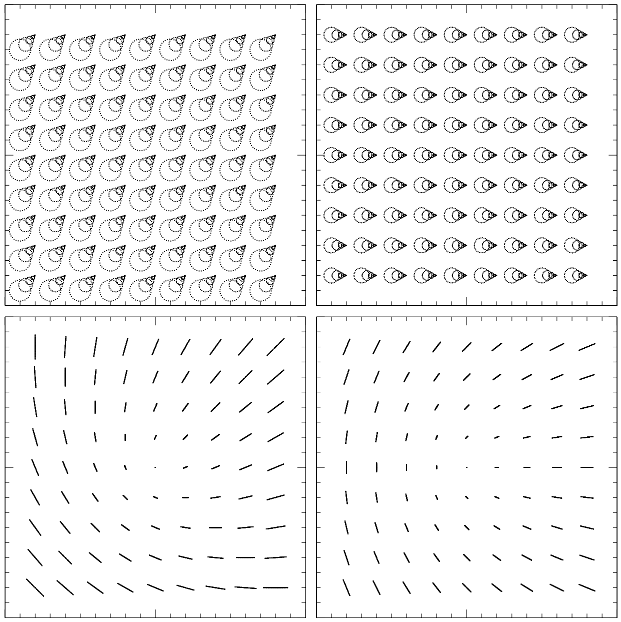

Fig. 17. *Top two panels*: spot diagrams for the misalignment coma with different misalignment directions. *Bottom two panels*: spot diagrams for the misalignment astigmatism with different misalignment directions. In both cases, the ellipticity parameter is scaled as $|e| \propto r^2$.

Let us start with the rotationally symmetric system. In this case, the wavefront distribution is given by (Thompson 2005)

$$\begin{aligned} W = &W_{040}\rho^4 + W_{131} h \rho^3 \cos\phi + W_{222} h^2 \rho^2 \cos^2\phi \\ &+ W_{220} h^2 \rho^2 + W_{311} h^3 \rho \cos\phi. \end{aligned} \tag{A1}$$

Among those five Seidel aberrations, ones that make an ellipticity parameter e non-zero are the Seidel coma (the second term) and astigmatism (the third term). The Seidel coma results in an ellipticity whose major axis oriented toward radial direction with $|e| \propto r^2$ where r is the distance from the center of image field. On the other hand, a combination of the astigmatism and field curvature (the fourth term) results in radially elongated (if $|W_{222}+W_{220}| > |W_{220}|$) or tangentially elongated (if $|W_{222}+W_{220}| < |W_{220}|$) ellipticity parameter with $|e| \propto r^4$ (see Fig. 16).

Next, we consider the case without rotational symmetry, allowing for a tilt and decenter between the axes of the exit pupil and image field. To compute the wavefront distribution in a perturbative approach, it is customary to introduce a vector $\vec{\sigma}$ with $(\sigma_x, \sigma_y) = (\sigma \sin\theta, \sigma \cos\theta)$ which represents the decentration of the center of the aberration field W with respect to the unperturbed field center. In this case, optical aberrations result in a PSF with non-zero ellipticity parameter are the *misalignment* coma and astigmatism.

The wavefront distribution for the misalignment coma is given by

$$W \propto \sigma \rho^3 \cos(\phi - \theta). \tag{A2}$$

In this case, the PSF has the same coma shape as the Seidel coma. However, the PSF does not depends on the position in the image field as the above expression does not include h, but the PSF (and thus the ellipticity) is constant over the image field as shown in the two top panels of Fig. 17.

The wavefront distribution for the misalignment astigmatism is given by

$$W \propto \sigma h \rho^2 \cos^2(\phi - \theta/2). \tag{A3}$$

In this case, the ellipticity of PSFs depends not only on the distance from the center of the image field but also on the azimuth angle (we shall denote it by ψ), and is written by $(e_1, e_2) \propto (r^2\cos(\psi-\theta), r^2\sin(\psi-\theta))$ (see Fig. 17).

Although an actual optical aberration may result in more complicated PSF than that expected from the third-order optical aberrations, it may be reasonable to build a model of the PSF ellipticity caused by optical aberration based on the above results. We consider the following form of a model (already introduced in eq. (7) but rewritten for self-contained) that consists three terms, namely the constant, axis-symmetric and asymmetric components;

$$\begin{pmatrix} e_1 \\ e_2 \end{pmatrix} = \begin{pmatrix} c_1 \\ c_2 \end{pmatrix} + \sum_{n_s} s_{n_s} r^{n_s} \begin{pmatrix} \cos 2\psi \\ \sin 2\psi \end{pmatrix}$$
$$+ \sum_{n_a} a_{n_a} r^{n_a} \begin{pmatrix} \cos(\psi-\theta) \\ \sin(\psi-\theta) \end{pmatrix}.$$

We determine the model parameters s_{n_s}, a_{n_a} and θ by the standard least square method with observed PSF ellipticities. In doing so, we take $n_s = \{1,2,3,4\}$ and $n_a = \{1,2\}$. As was shown in §3, this simple model succeeds very well in fitting the global pattern of PSF ellipticities in Suprime-Cam data.

Appendix 2. A numerical study of PSF ellipticities caused by atmospheric turbulence

We examine statistical properties of PSF ellipticities caused by atmospheric truculence using a numerical simulation. The aim of this study is to investigate the shape and amplitude of the power spectrum of atmospheric PSF ellipticities, which is an essential knowledge for understanding statistical properties of PSF ellipticities. Our approach is similar to one taken by Jee & Tyson (2011), that is to utilize a numerical simulation of wave propagation through atmospheric turbulence for evaluating atmospheric PSFs.

Here we briefly describe our numerical simulation. Since we heavily use a publicity open software ARROYO (Britton 2004), we refer the reader to the above reference and software documents[6] for details of models, computational methods and their implementation. The atmospheric turbulence is modeled by eleven-layer frozen Kolmogorov screens with the atmospheric model at Mauna-Kea proposed by Ellerbroek & Rigaut (2000). The strength of the total atmospheric turbulence is set by the Fried length r_0 for which we adopt a value proposed by Ellerbroek & Rigaut (2000); $r_0 = 0.23$m at a wavelength of 0.5μm. Neither a large scale nor small scale cutoff (the, so-called, outer and inner scale) on the Kolmogorov power spectrum is imposed. The wind model given by eq. (3.20) of Hardy (1998) is adopted with random wind directions. Having the atmospheric model ready, an atmospherically disturbed phase function of a wavefront is computed. We consider a monochromatic electromagnetic wave with wavelength of 0.8μm. Then, an instantaneous PSF is obtained by Fourier transforming the phase function within a pupil for which we assume a circular pupil with 8.2m diameter for simplicity. All the above models and computations are implemented in ARROYO subroutines. Finally, a sequence of instantaneous PSFs are added to obtain a long-exposure PSF. We compute PSFs of 1, 10 and 60 seconds exposures on 64×64 regular grids over a $30' \times 30'$ focal plane.

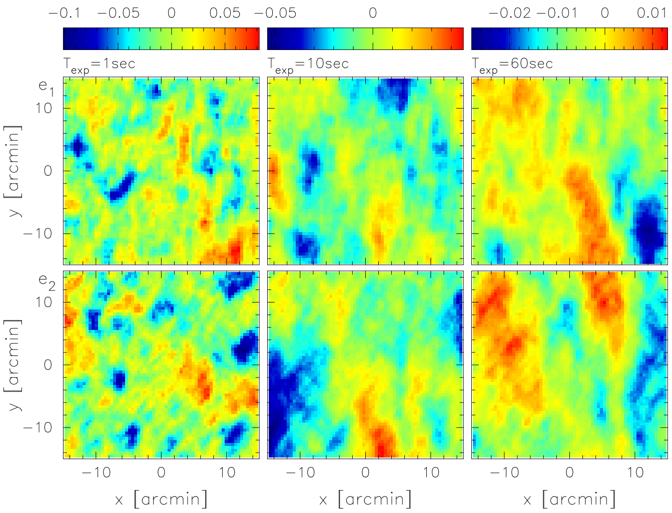

Fig. 18. Ellipticity magnitude obtained from the numerical simulation described in Appendix 2: upper and lower panels are for e_1 and e_2, respectively, and the color scales are displayed on the top of those panels. The exposure times are, from left to right, 1-sec, 10-sec and 60-sec, respectively.

We generate 20 realizations. The mean FWHM of PSFs among the realizations is 0.65 arcsec for 60 seconds exposure which is in a good agreement with the observed value at Subaru telescope (Miyazaki et al. 2002). For an illustrative example, one realization is shown in Figure 18, where the ripple like feature appears. Similar features are observed in CFHT data (Heymans et al. 2012) and Suprime-Cam data (see Figs 6 and 7). It should be however noted that the appearance varies widely between realizations depending on turbulence and wind properties.

We measure the power spectrum and aperture mass variance from the simulation data and present in Figure 19 and 20, respectively. The following three major findings are derived from the Figures: First, the amplitude of the power spectrum decreases as $P_e \propto T_{exp}^{-1}$ as was already pointed out in previous studies (Wittman 2005; de Vries et al 2007; Jee & Tyson 20011; Chang et al. 2012; 2013

---

[6] http://eraserhead.caltech.edu/arroyo/arroyo.html

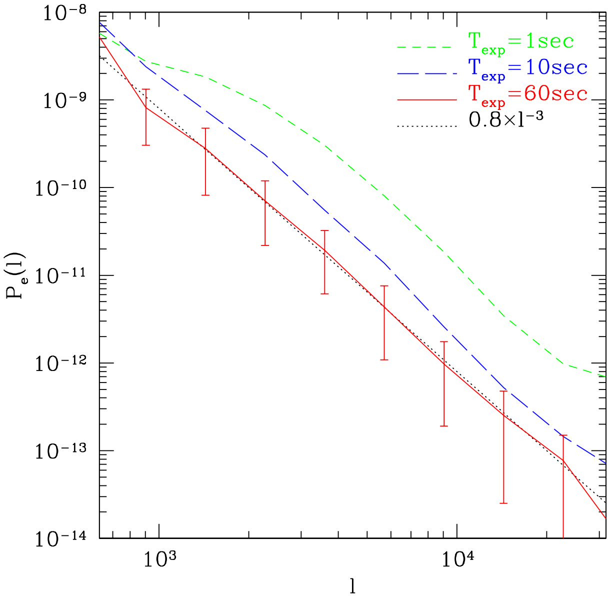

Fig. 19. The power spectrum of PSF ellipticities measured from the simulation results. The dashed, long-dashed and solid lines are for 1-sec, 10-sec and 60-sec exposures, respectively. The error bars, plotted only for the 60-sec result for clarify, show the RMS among 20 realizations. The dotted line shows the power-law model of $P_e(l) = 0.5 \times l^{-3}$ which turns out to be a good approximation of the 60-sec result.

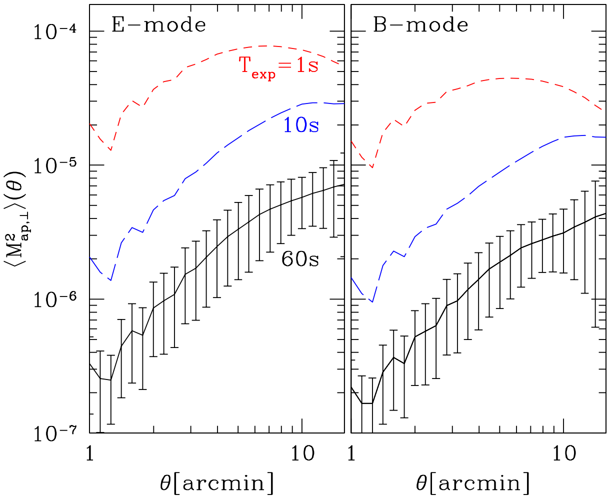

Fig. 20. The aperture mass variance of PSF ellipticities measured from the simulation results. The dashed, long-dashed and solid lines are for 1-sec, 10-sec and 60-sec exposures, respectively. The error bars, plotted only for the 60-sec result for clarify, show the RMS among 20 realizations.

Heymans et al. 2012). Second, the power spectrum is approximated by a power-law model with the power index of −3. A plausible reason of the power-law shape is our assumption of the power-law turbulence power spectrum without a cutoff. In reality, a large-scale cutoff (the, so-called, outer scale) at around 10−100m is expected (e.g., Hardy 1998), which may result in a cutoff in the PSF ellipticity power spectrum at a scale around 1 degree. Third, the atmospheric turbulence results in E/B-mode almost equally partitioned PSF ellipticities. At a closer look at Fig. 20, one may however find that the E-mode amplitude is slightly but systematically larger than B-mode. A reason of this is unclear and we leave it for future work.

In addition to the above findings, we also find from Figs. 19 and 20, that models $P_e(l) \sim 0.8 l^{-3}$ and $\langle M^2_{ap,\perp}\rangle(\theta) \sim 4 \times 10^{-7}\theta$ give a good fit to the 60-sec result. In what follows, we discuss how those correlation amplitude depends on other observational parameters including the exposure time and the atmospheric seeing FWHM ($\theta_{\rm atm}$). Consider a case $D \gg r_0$ where D denotes a diameter of a telescope, and a monochromatic radiation with a wavelength λ from a point source. A wavefront from a point source is disturbed by atmospheric turbulence, and we consider, for simple approximation, the disturbed wavefront as segmented r_0-sized patches of constant phase and random phases between the individual patches (Saha 2007, and see e.g., Fig 5.3 of that textbook for an illustration). The number of patches within a pupil is approximately $N_{patch} \sim (D/r_0)^2$. A wavefront from each patch results in a sharp speckle PSF on a focal plane, and a total PSF is viewed as a superposition of randomly distributed speckles over an extent of the atmospheric seeing size $\theta_{\rm atm} \sim \lambda/r_0$ (Hardy 1998; Saha 2000; see for illustrative examples, Fig 3 of Kaiser, Tonry & Luppino 2000; and Fig 5 of Jee & Tyson 2011). In this picture, the PSF anisotropy is understood as a natural consequence of a finite number of speckles. Since the disturbed wavefront changes quickly, more different speckles are accumulated as $N_{spec} \propto T_{exp}$, and thus the PSF becomes rounder. It is found from the above numerical simulation that the RMS of PSF ellipticities decreases as $\langle e^2\rangle^{1/2} \propto T_{exp}^{-1/2}$, which combined with the above mentioned relationships leads to the following relationships;

$$\begin{aligned}\langle e^2\rangle^{1/2} &\propto N_{spec}^{-1/2} \propto T_{exp}^{-1/2} N_{patch}^{-1/2}\\ &\propto T_{exp}^{-1/2} r_0 \propto T_{exp}^{-1/2}/\theta_{\rm atm}.\end{aligned}$$

We test this relationship against numerical simulations with different values of r_0, from which the above dependences of r_0 and $\theta_{\rm atm}$ on $\langle e^2\rangle^{1/2}$ are verified. Combined the last relationship with the power-law fitting models, we have

$$P_e(l) \sim 0.8 \times l^{-3} \times \left(\frac{T_{exp}}{1\rm min}\right)^{-1} \left(\frac{\theta_{\rm atm}}{0.65\rm arcsec}\right)^{-2}, \quad (A4)$$

and

$$\langle M^2_{ap,\perp}\rangle(\theta) \sim 4 \times 10^{-7} \times \theta$$

$$\times \left(\frac{T_{exp}}{1\mathrm{min}}\right)^{-1} \left(\frac{\theta_{\mathrm{atm}}}{0.65\mathrm{arcsec}}\right)^{-2}. \qquad \text{(A5)}$$

Although the above relationships are quite crude, those are useful to quickly evaluate a magnitude of atmospheric PSF ellipticities for a given set of observational parameters. Note that these relationships are valid only for a telescope with a diameter of 8.2m. It may be worth pointing out that it is found from numerical simulations with different telescope diameters that the amplitude of PSF ellipticities is insensitive to D. This differs from a scaling relationship of $P_e \propto D^2$ expected from the above consideration (likewise for $\langle M_{ap,\perp}^2 \rangle$). This difference may be explained by the diameter dependence of the PSF which is not taken into account in the above consideration. According to the diffraction theory (e.g., Hardy 1998; Saha 2007), the PSF is the inverse Fourier transform of the optical transfer function (OTF) which is the auto correlation function of the product of the telescope pupil function with the atmospheric phase function. In that relationship, the diameter of telescope enters through the pupil function. Therefore, roughly and intuitively speaking, the power spectrum of PSF ellipticities relates to the OTF, and the diameter acts as a large-scale cutoff. Since the turbulence power spectrum has a larger power on a larger scales (Kolmogorov power spectrum has the shape of $k^{-11/3}$), the large-scale cutoff imposed by the telescope diameter may have a great impact on the amplitude of PSF ellipticities.